3
Hot spots, swells and mantle plumes

Peter Olson
Department of Earth and Planetary Sciences,
The Johns Hopkins University,
Baltimore, MD 21218, USA

Abstract

Fluid mechanical models are used to describe the evolution of a mantle plume, from initiation as a thermal boundary layer instability to its intrusion into the lithosphere. It is argued that the plume theory explains many of the distinctive properties of hot spots and hot-spot volcanism. According to the plume theory, hot spots are initiated by the intrusion of large mantle diapirs into the lithosphere, originating from a hot thermal boundary layer, perhaps the D" layer at the base of the mantle. These diapirs may be the source for massive continental flood-basalt eruptions and for oceanic plateau basalts. Fluid dynamical considerations indicate that fully developed mantle plumes consist of narrow conduits of hot, buoyant material, perhaps partially molten. Mantle conduit structures permit a variety of propagating wave disturbances and instabilities capable of transporting mass and heat rapidly from the source boundary layer to the lithosphere, and producing time variability in hot spot eruption volumes and compositions. Finally, a new interpretation is given to topographic swells associated with hot-spot tracks. It is argued that hot-spot swells represent the surface response to buoyant plumes refracted horizontally by the lithosphere. A model is derived for plumes spreading from a localized conduit source beneath moving lithosphere. The model predicts that the shape of refracted plumes and the isostatic topography they support is determined by a balance between longitudinal advection by the moving plate and lateral spreading in the asthenosphere. The plume structure is governed by a single dimensionless parameter, the *intrusion number* $I = (g'Q)(96\pi\nu_p u_m^2)$, where g', Q and ν_p are the plume buoyancy, discharge and kinematic viscosity, respectively, and u_m is the plate speed. It is shown that the topography of major hot-spot swells, such as the Hawaiian Ridge, can be modeled by refracted plumes with intrusion numbers in the range $I = 0.3$–1.0. Plumes with larger intrusion numbers produce broad, dome-shaped swells beneath moving plates, while steady state plumes with smaller intrusion numbers produce narrow, ridge-shaped swells.

Contents

Notation

		Units
A	conduit area	m^2
G	6.6732×10^{-11}	$N\,m^2\,kg^{-1}$
I	intrusion number	
L	intrusion length-scale	m
M	swell magnitude	$m^3\,s^{-1}$
ΔN	geoid anomaly height	m
P	conduit pressure	$N\,m^{-2}$
Q	conduit volume flux	$m^3\,s^{-1}$

Magma Transport and Storage. Edited by M.P. Ryan

R	diapir radius	m
R_s	diapir separation radius	m
Ra	Rayleigh number	
Ra_c	critical Ra	
Ra_δ	local Ra	
S	intrusion thickness	m
T	temperature	K
ΔT	boundary layer temperature rise	K
U_∞	Stokes speed	$m\,s^{-1}$
V	diapir volume	m^3
ΔV	wave volume	m^3
Z	plate thickness	m
c	conduit wave speed	$m\,s^{-1}$
g	gravity	$m\,s^{-2}$
g'	buoyancy	$m\,s^{-2}$
h	swell topography	m
i,j	grid indices	
q	horizontal plume flux	$m^2\,s^{-1}$
t	time	s
t_c	instability onset time	s
t	diapir separation time	s
Δt	conduit wave duration	s
u_m	plate velocity	$m\,s^{-1}$
u_p	plume velocity	$m\,s^{-1}$
x,y,z	coordinates	m
x_p	conduit position	m
α	thermal expansion coefficient	K^{-1}
δ	boundary layer thickness	m
η_p	plume dynamic viscosity	$N\,m^{-2}\,s$
$\varkappa$	thermal diffusion coefficient	$m^2\,s^{-1}$
λ	conduit wavelength	m
ν	mantle kinematic viscosity	$m^2\,s^{-1}$
ν_p	plume kinematic viscosity	$m^2\,s^{-1}$
π	3.1415926...	
ρ	mantle density	$kg\,m^{-3}$
ρ_w	sea-water density	$kg\,m^{-3}$
$\Delta\rho$	plume density deficit	$kg\,m^{-3}$
σ	intrusivity	$m^{-1}\,s^{-1}$
τ_n	normal stress	$N\,m^{-2}$

1. Hot Spots, Ocean Island Basalts, Sea-floor Swells and the Mantle Plume Model

It has been recognized for more than two decades that hot spots represent a distinct form of tectonic activity. Hot-spot volcanism is not a product of sea-floor spreading, the dominant process for generating basaltic magmas in the mantle. Whereas mid-ocean ridge basalts (MORB) are formed by partial melting of mantle peridotites previously depleted in incompatible trace elements, ocean island basalts (OIB) produced at hot spots often lack the depletion in trace elements that characterizes MORB and its parent mantle material (Zindler and Hart, 1986). Isotopic compositions suggest that OIB is derived from a complex mixture of sources, including primitive mantle, the depleted MORB source, and perhaps recycled oceanic crust (Chase, 1981; Hofmann and White, 1982; Hart, Gerlach and White, 1986). Geophysical evidence for a hot-spot source mechanism separate from plate tectonics is equally compelling. Mid-ocean ridge basalts are a product of pressure-release melting within large-scale upwellings beneath actively spreading ridges, with most of the material in the upwelling coming from the upper mantle (Silver, Carlson and Olson, 1988). In contrast, the source for hot-spots evidently lies deeper in the mantle. Numerous analyses of hot-spot track and plate-motion directions have established that hot spots are nearly stationary for time intervals of 50–100 million years (Morgan, 1983; Jurdy and Gordon, 1984; Molnar and Stock, 1987). There are several examples preserved in the ocean crust of migrating ridges having passed through hot spots without terminating the hot-spot activity (Morgan, 1981).

Both in terms of magmatic activity and their contribution to mantle heat transfer, hot spots are a secondary source of melting, compared with the global mid-ocean ridge system. At the present time, basaltic crust is produced at a rate of $18\ km^3\,year^{-1}$ at spreading centres (Basaltic Volcanism Study Project, 1981), while only about $0.5\ km^3\,year^{-1}$ year is currently produced by hot spots (Richards, Duncan and Courtillot, 1989). Similarly, the normal cooling of the oceanic lithosphere accounts for approximately 3×10^{13} W of heat loss, while the anomalous heat flux associated with hot spots and hot-spot swells is at least an order of magnitude smaller (Davies, 1988). However, the relative strengths of the two sources, as implied by present-day heat flow and eruption rates, is not the whole story, because there is good evidence that volcanism related to hot spots is strongly variable in time. Extremely

high rates of volcanism are associated with initiation of hot spots, and with the resurgence of existing ones (Vogt, 1979). Initiation or resurgence produces continental flood basalts at hot spots located within the continental lithosphere, and ocean plateaus in the oceanic lithosphere (White and McKenzie, 1989; Richards, Ducan and Courtillot, 1989).

The best indication of the source volume involved in hot-spot volcanism is the association of hot spots with large topographic rises, the hot-spot swells. Hot-spot swells are regional-scale topographic highs, typically 1000 km across, with up to 3 km anomalous elevation, distributed symmetrically about the hot spot track (Crough, 1978). Positive geoid anomalies over swells indicate compensation by anomalously low-density mantle material at depths of 50–100 km (Sandwell and MacKenzie, 1989). Small, positive heat-flow anomalies have been measured on the flanks of oceanic hot-spot swells, indicating the presence of high temperatures within and below the lithosphere (Detrick *et al.*, 1981, 1986).

In this chapter, we show that swells can be interpreted as the surface response to the intrusion of large volumes of buoyant plume material into the upper mantle beneath the rigid portion of the lithosphere. According to this interpretation of hot-spot swell formation, most of the source material for hot-spot volcanism accumulates near the base of the lithosphere, where the plume is horizontally refracted, and never reaches the surface. The intrusion rate of plume material needed to support major swells is believed to be quite large—in the range of 6 $km^3\,year^{-1}$ for the Hawaiian hot-spot, roughly 100 times the current volcanic eruption rate (Bargar and Jackson, 1974). At other hot spots, the implied ratio is even larger. It suggests that the melt fraction within the plume material is extremely small on average, or more likely, the efficiency of magma extraction is so low that most of the melt produced in a rising plume is trapped beneath the rigid part of the lithosphere. The same model also predicts that much of the anomalous heat from the plume accumulates at sublithospheric depths, and can only reach the surface through the slow and relatively inefficient mechanism of heat conduction. This is a possible explanation for why heat flow on sea-floor swells is only slightly above the background value for normal sea floor of the same age (Von Herzen *et al.*, 1982).

2. Boundary Layer Instabilities and Plume Formation

Thermal plumes form by instability of hot thermal boundary layers, a fact that severely constrains the possible source regions for plumes in the mantle. The temperature structure of the mantle, including the location of hot thermal boundary layers, is controlled by the structure of the large-scale subsolidus thermal convection. One region in the mantle where there is compelling evidence for a hot thermal boundary layer is the layer D", just above the core–mantle boundary (Olson, Silver and Carlson, 1990). The argument for a thermal boundary layer at the bottom of the mantle is based on the mismatch between lower mantle and core adiabats, which indicates a 300–1000 K superadiabatic temperature rise across D" (Jeanloz and Morris, 1986). Plumes originating from D" are predicted by models of whole mantle convection (Loper, 1985; Bercovici, Schubert and Glatsmaier, 1989). Another region where plume formation is possible is the base of the transition zone, where uncertainty in the lower mantle geotherm allows for the existence of a superadiabatic interfacial thermal layer between the upper and the lower mantle (Jeanloz and Morris, 1986). An interfacial thermal layer near the base of the transition zone is predicted by models of layered mantle convection (Richter and McKenzie, 1981). The mechanics of boundary layer instability are for the most part governed by local conditions in the thermal layer, so it is not necessary to be specific about the depth of the source layer in a model of the early stages of plume development.

2.1. Thermal boundary layer instability

The global Rayleigh number of mantle convection is in the range 5×10^5–5×10^7, the lower figure appropriate for layered convection, the upper one for the whole mantle convection. Either value is sufficiently high that mantle convection is intrinsically time-dependent (Machetel and Yuen, 1986; Bercovici, Schubert and Glatsmaier, 1989). An important element in time-dependent convection is the repeated generation of instabilities in the thermal boundary layers. In fully developed time-dependent convection, the instabilities form thermal plumes, which separate from the

boundary layers and become secondary scale components of the motion. Certain dynamical conditions must be met before instabilities in a thermal boundary layer are possible. Furthermore, if these instabilities are to develop into plumes, they must grow to a critical size in a time that is shorter than the mean residence time of material in the boundary layer. The following rudimentary model provides estimates of the time-scales involved in each of these steps.

The criterion for onset of local instability depends most strongly on the boundary layer Rayleigh number Ra_δ, defined as

$$Ra_\delta = \frac{\alpha g \Delta T \delta(t)^3}{\kappa \nu} \quad (1)$$

where α is thermal expansivity, g is gravity, ΔT is the superadiabatic temperature rise across the thermal boundary layer, $\delta(t)$ is the local boundary layer thickness which depends on the time t spent in the layer, κ is thermal diffusivity and ν is kinematic viscosity. The boundary layer grows by diffusion according to

$$\delta(t) = (\pi \kappa t)^{1/2} \quad (2)$$

Howard (1964) proposed that instability occurs when the local Rayleigh number reaches a critical value, Ra_c

$$Ra_\delta = Ra_c \quad (3)$$

where $Ra_c \simeq 3 \times 10^3$. Solving for t in equations (1)–(3) yields the onset time for boundary layer instabilities

$$t_c = \frac{1}{\pi \kappa^{1/3}} \left(\frac{\nu Ra_c}{\alpha g \Delta T} \right)^{2/3} \quad (4)$$

Expression (4) predicts rather fast onset times for mantle boundary layer instabilities. Using $\kappa = 10^{-6}\,\mathrm{m^2\,s^{-1}}$, $\alpha \Delta T g = g' = 10^{-1}\,\mathrm{m\,s^{-2}}$, and $\nu = 2 \times 10^{16}\,\mathrm{m^2\,s^{-1}}$ gives $t_c = 70$ Ma. This value is derived using a typical estimate for the viscosity in the D″ layer. Longer onset times would result if a larger viscosity value, appropriate for the lower mantle (Hager, 1984) were used. The result indicates that growing perturbations are likely to be produced near the base of the mantle, particularly if low viscosities are present in the thermal boundary layer; a conclusion that is consistent with numerical experiments on the stability of the D" layer (Christensen, 1984).

The presence of growing perturbations does not automatically ensure plume formation, because the growth times may not be short compared with the total residence time in the thermal boundary layer. Generally, the growth rate of an instability depends inversely on the local viscosity, so that strong temperature dependence of viscosity promotes the growth of instabilities in hot thermal boundary layers. Numerical simulations indicate that instabilities can grow into starting plumes in the D" layer on time-scales of 50–100 Ma provided that the viscosity in the boundary layer is several orders of magnitude less than the lower mantle average (Olson, Schubert and Anderson, 1987). The growth mechanism involves coalescence of numerous small perturbations, to form a disturbance large enough to separate from the thermal boundary layer.

Figure 1 shows plume formation in a hot thermal boundary layer at the base of a fluid layer with strongly temperature-dependent viscosity. The figure shows isotherm contours from a numerical experiment designed to model instability and plume initiation in the D" layer, for the case of a purely thermal boundary layer. The incipient plumes form as diapirs, growing by influx of hot, low-viscosity fluid from the thermal boundary layer. Since there is no large-scale circulation from other sources in Figure 1, all of the motion is due to the instabilities themselves, and the diapirs begin to separate from the layer when their speed of buoyant ascent exceeds their growth rate. The calculations in Figure 1 are two-dimensional; the evolution of three-dimensional diapirs follows the same sequence as shown here

Figure 1. (opposite) Temperature contours at selected times from a two-dimensional numerical calculation of plume formation in the thermal boundary layer at the base of the mantle (Olson, Schubert and Anderson, 1987). In the calculation, the temperature of the lower surface, representing the core–mantle boundary, is fixed at 3773 K, and the interior, representing the deepest 400 km of the lower mantle, is initially at 2973 K. The horizontal and vertical divisions are 200 and 100 km, respectively, and the contour interval is 44.4 K. Other model parameters: density $5.5 \times 10^3\,\mathrm{kg\,m^{-3}}$, thermal expansion coefficient $3 \times 10^{-5}\,\mathrm{K^{-1}}$, thermal diffusivity $1 \times 10^{-6}\,\mathrm{m^2\,s^{-1}}$. The lower mantle has a temperature-dependent subsolidus viscosity (Arrhenius law), which varies from 10^{22} Pa s at 2973 K to 10^{19} Pa s at 3773 K. Shown are the following stages in plume development: (a) diffusive thermal boundary layer growth at 31.7 Ma; (b) small amplitude instability at 76.2 Ma (c) diapir growth at 88.9 Ma; (d) diapir separation at 108 Ma

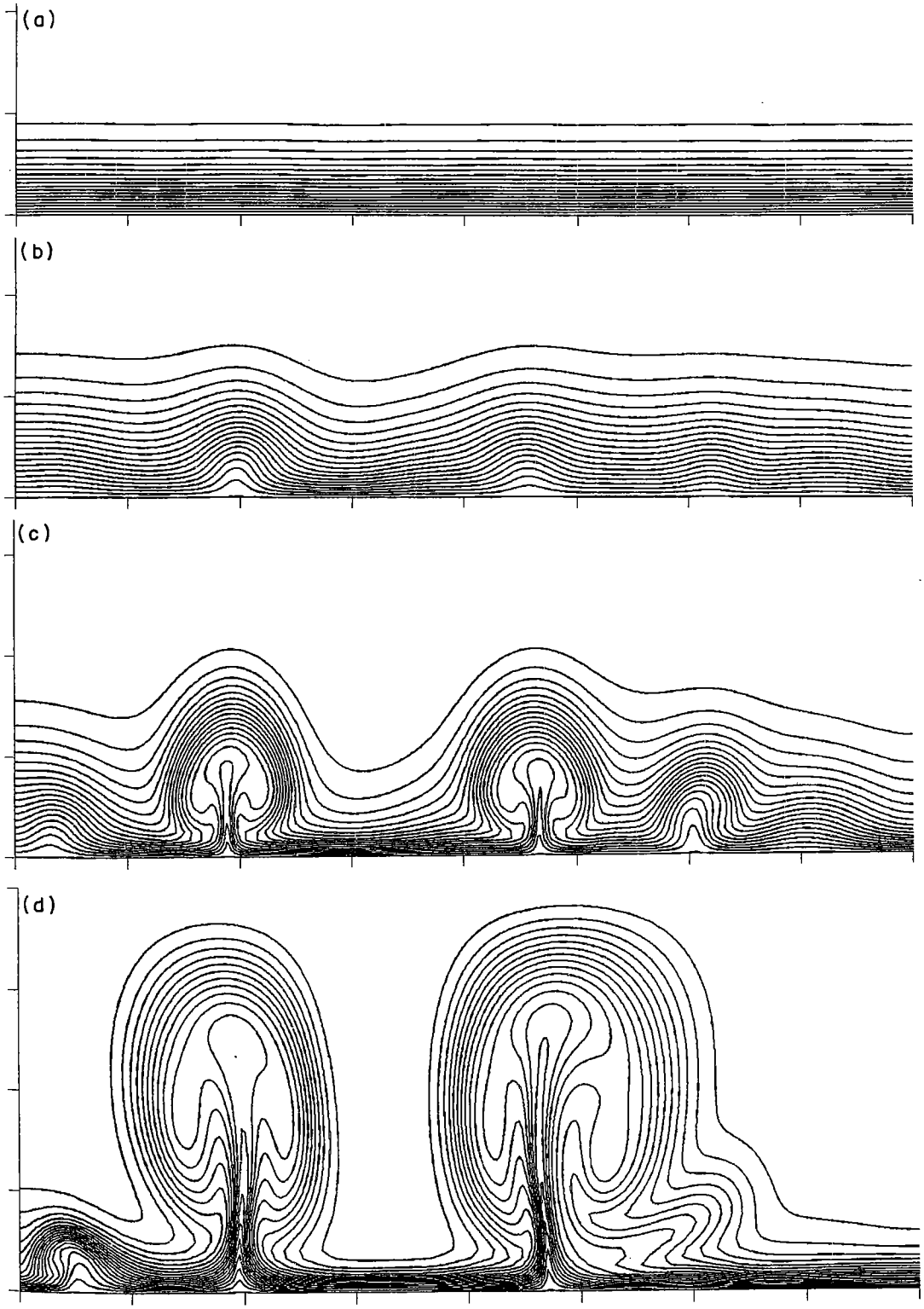

Figure 1. (*caption opposite*)

in two dimensions, but develop faster in the later stages.

The conditions for separation can be obtained from the following simple model, first proposed by Whitehead and Luther (1975). Denoting the rate of influx of hot fluid into one of these diapirs by Q, the rate of increase of diapir volume V is just

$$\frac{dV}{dt} = Q \tag{5}$$

and the diapir radius R grows according to

$$\frac{dR}{dt} = \frac{Q}{4\pi R^2} \tag{6}$$

The ascent speed can be modeled by the Stokes velocity of a buoyant fluid sphere in an infinite, more viscous exterior fluid:

$$U_\infty = \frac{g' R^2}{3\nu} \tag{7}$$

where $g' = g\Delta\rho/\rho$ is the diapir buoyancy and ν is the kinematic viscosity of the exterior fluid. Here, $\Delta\rho = \rho - \rho_p$ is the density difference between the exterior mantle and the diapir, and is assumed constant in this derivation. Separation occurs when equation (7) exceeds (6), so that

$$R_s = \left(\frac{3\nu Q}{4\pi g'}\right)^{1/4} \tag{8}$$

and

$$t_s = \left(\frac{4\pi}{3Q}\right)^{1/4} \left(\frac{\nu}{g'}\right)^{3/4} \tag{9}$$

are the radius at separation and the required inflation time.

Because of the large viscosity of the mantle, starting plumes require large diapirs for separation from the hot thermal boundary layer. A numerical estimate demonstrates this point. At the present time, the Hawaiian swell is supported by a mass flux of approximately $200\ m^3\ s^{-1}$ (Davies, 1988). Assuming a diapir buoyancy $g' = 0.1\ m\ s^{-2}$ and $\nu = 2 \times 10^{18}\ m^2\ s^{-1}$ for the kinematic viscosity in the lower mantle, (8) and (9) predict $R_s = 180$ km and $t_s = 3.6$ Ma. These estimates are by no means precise, but they indicate three important attributes of mantle plumes: first, buoyant plumes originating from the deep mantle necessarily have large volumes, second, the time required for separation, once a plume diapir beings to form in the thermal boundary layer, is generally shorter than the time required for the initial instability to develop, and third, the entire process of plume formation can occur within about 100 Ma.

2.2. The role of chemical heterogeneity

The analysis in the previous section is based on the assumption that only thermal buoyancy effects are important in mantle plume formation. In fact, there is mounting evidence that chemical heterogeneity is responsible for much of the seismic heterogeneity in the D" layer. If plumes indeed originate near the base of the mantle, then chemically induced buoyancy may play a significant role.

The best evidence for chemical heterogeneity in the D" layer is from body wave seismology. That evidence consists of a set of arrivals intermediate between shear wave phases S and SKS, which have been interpreted by T. Lay and co-workers as refractions from a mantle discontinuity, with a 3% shear-wave velocity increase, located approximately 280 km above the core–mantle boundary. The findings from several regional studies of this arrival are reviewed by Young and Lay (1987). Between this discontinuity and the core–mantle boundary, the S-wave velocity profile has either a negative gradient or a reduced positive gradient relative to the Earth model PREM. In order for models with this discontinuity to match S-wave travel times, a layer of reduced velocity gradient above the discontinuity is also required. Thus, the preferred structure of the D" layer derived from shear waves consists of a discontinuity with a 3% velocity increase, imbedded within a layer of reduced (or even locally negative) velocity gradients several hundred kilometers thick. Global-scale variations in the thickness of this layer are well established (Young and Lay, 1987).

The simplest interpretation of this structure is a thick thermal boundary layer stabilized by a step increase in density due to composition, corresponding to the S-wave refractor. The dynamical behavior of such a thermo-chemical boundary layer has been investigated by Hansen and Yuen (1988), using a numerical model of doubly diffusive convection. Hansen and Yuen (1988) found that a large density increase, approximately 3%, is required to stabilize this structure in the presence of mantle convection. A density increase of this magnitude could be produced by iron enrichment;

however, iron enrichment would produce a shear-wave velocity decrease, which is inconsistent with the seismic data. An alternative explanation is silica enrichment, which would result in the required velocity increase, but would not increase the density. If this is the explanation, then plumes from the D" layer would be enriched in silica, at least relative to the lower mantle. A petrological test of the validity of either of these hypotheses is to detect silica or iron enrichment in the source material of hot spot volcanics.

3. Plume Diapirs and Conduits

3.1. Starting plumes

The morphology of fully developed plumes in the mantle is governed by the viscosity contrast between the plume and mantle, and also by the interaction of the plume with the background mantle circulation through which the plume must ascend. Figure 2 shows the structure of a starting plume ascending through a much more viscous matrix fluid, which, except for the motion induced by the plume, is at rest. The plume consists of a leading diapir and a thin conduit connecting the diapir with the source region at depth. Low-viscosity fluid ascends through the conduit as laminar, parabolic Poiseuille flow in a circular pipe. The flow rate is initially much faster than the ascent speed of the diapir, so the diapir inflates and accelerates. Eventually an equilibrium is reached in which the speed of the diapir equals the average speed of fluid in the conduit. This represents the maximum size the diapir can reach, unless entrainment of the surrounding viscous fluid into the plume occurs.

The approach to equilibrium size can be estimated from the following model, originally formulated by Whitehead and Luther (1975). As the diapir ascends, its rate of volume increase equals the difference between the volume flux at the source and the rate at which the new conduit forms. The appropriate generalization of equation (5) is

$$\frac{dV}{dt} = Q - AU_\infty \tag{10}$$

where A is the cross-sectional area of the conduit. Using $dt = dz/U_\infty$, where z is the vertical coordinate, equation (10) becomes

$$\frac{dV}{dz} + A = \frac{Q}{U_\infty} \tag{11}$$

This equation can be solved numerically using the separation radius (equation (8)) to compute the initial volume. There are two limiting cases of this equation that admit analytical solution. One is the terminal condition,when the first term in equation (11) vanishes. The conduit area appearing in equation (11) can be expressed in terms of the discharge Q by assuming laminar, parabolic, buoyantly driven Poiseuille flow of the conduit fluid, for which

$$A = \left(\frac{8\pi\nu_p Q}{g'}\right)^{1/2} \tag{12}$$

where ν_p is the plume kinematic viscosity. Combining equations (11) and (12) in this limit yields

$$U_\infty = \left(\frac{g'Q}{8\pi\nu_p}\right)^{1/2} \tag{13}$$

for the terminal ascent speed, and assuming Stokes law (equation (7))

$$V_\infty = \frac{4\pi}{3}(3\nu)^{3/2}\left(\frac{Q}{8\pi g'\nu_p}\right)^{3/4} \tag{14}$$

for the terminal volume. The other case of interest occurs when the conduit volume is negligible compared with the diapir volume. Ignoring the conduit area A in equation (11) and using equation (8) to give the initial volume yields, upon integration

$$V(z) = \left[\left(\frac{4\pi}{3}\right)^{5/3}\left(\frac{3\nu Q}{4\pi g'}\right)^{5/4} + \left(\frac{4\pi}{3}\right)^{2/3}\left(\frac{5\nu Q z}{g'}\right)\right]^{3/5} \tag{15}$$

and the corresponding time required to rise a distance z is

$$t(z) = \frac{1}{3}\left(\frac{4\pi}{Q}\right)^{2/5}\left(\frac{15z\nu}{g'}\right)^{3/5} \tag{16}$$

Following an early suggestion by Morgan (1981), both White and McKenzie (1989) and Richards, Duncan and Courtillot (1989) have recently proposed that massive flood basalt eruptions are the result of extrusion of melt from the leading diapir of a mantle plume as it intrudes the lithosphere from below. According to this interpretation, flood basalt eruptions mark the initiation of a hot-spot track. Richards, Duncan and Courtillot (1989) argue that four continental

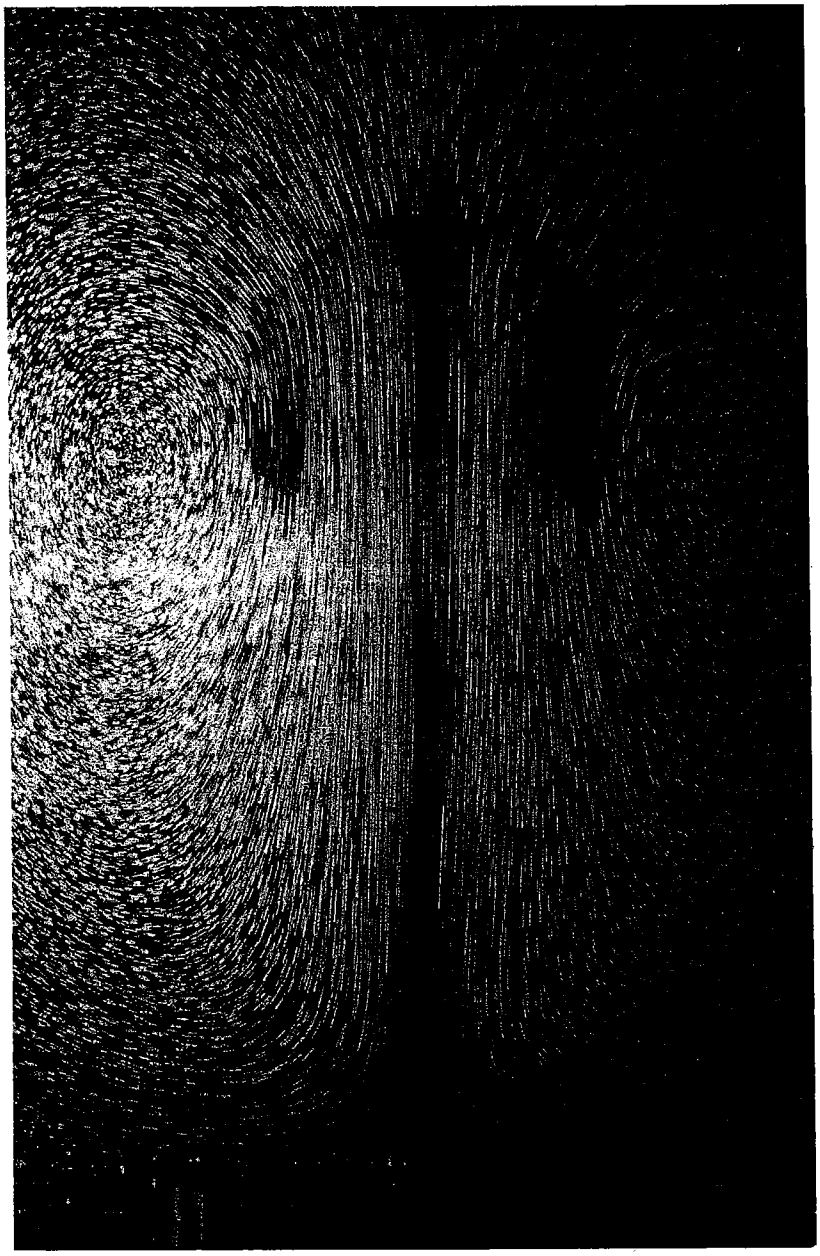

Figure 2. Time-lapse exposure showing flow-field (streaks) and thermal field (shadow) of a starting thermal plume above a heated disk in a temperature-dependent viscous sucrose solution (Singer, 1986). The disk is approximately 50 K hotter than the ambient fluid, and the viscosity varies from approximately 150 Pa s at the ambient temperature to 2 Pa s at the disk temperature. The vertical dimension of the plume is approximately 0.3 m. Note the large leading diapir and the narrow conduit structure

flood basalt provinces (Deccan, Tertiary North Atlantic, Parana and Karroo) represent the onset of currently active hot spots (Reunion, Iceland, Tristan da Cunha and Prince Edward), and that in each case nearly $2 \times 10^{15}\,m^3$ of magma was extruded within a few million years of hot-spot initiation.

This interpretation fits nicely with the starting plume model just described, as can be demonstrated by a simple numerical calculation using one of the two end-member cases. For most choices of mantle diapir parameters, terminal conditions are not expected to be reached during ascent, even across the whole mantle. The steadily

growing diapir model more likely applies to starting mantle plumes, and therefore equations (15) and (16) are the expressions to use.

Richards, Duncan and Courtillot (1989) attribute the Deccan flood basalts to the initiation of the Reunion hot-spot. In order to calculate the diapir volume associated with such an event, the source volume flux for the Reunion hot spot must be estimated. Table 1 gives hot-spot magnitudes recently compiled by Davies (1988), derived from swell heights and plate speeds. The swell magnitude M is related to the source discharge according to

$$M = \frac{\Delta\rho}{\rho} Q \qquad (17)$$

Assuming the plume–mantle density contrast $\Delta\rho/\rho = 0.01$, the data in table 1 give $Q = 39\ \mathrm{m^3\,s^{-1}}$ for the Reunion hot-spot. Using $\nu = 2 \times 10^{18}\ \mathrm{m^2\,s^{-1}}$, $g' = 0.1\ \mathrm{m\,s^{-2}}$ as before, and $z_m = 2.8 \times 10^6\ \mathrm{m}$ for the ascent distance from D'' to the lithosphere, equations (15) and (16) give $V(z_m) \simeq 1.2 \times 10^{17}\ \mathrm{m^3}$ and $t(z_m) \simeq 95$ Ma. The rather long ascent time reflects the large viscosity in the lower mantle. There is no difficulty accounting for the volume of magma needed to produce flood basalts by partial melting of mantle plumes. The estimated volume of basalts in the Deccan Traps, for example, represents only 1–2% of the diapir volume calculated for initiation of the Reunion hot spot.

3.2. Conduit waves and diapir chains

Plume conduits are dynamically stable structures provided the supply of low viscosity, buoyant material is continuous and the conduits are the only source of motion in the medium into which they are intruding. However, this is not the case in the mantle, where plumes must coexist with the large-scale flow associated with plate motions. Larger scale motions in the mantle deform the smaller scale conduit structures, producing a

Table 1. Hot-spot swell parameters

Hot-spot	Magnitude ($\mathrm{m^3\,s^{-1}}$*)	Plate speed ($\mathrm{mm\,year^{-1}}$)	Intrusion number ($\times 10^{20}\,\eta_p^{-1}$)†	Length-scale (km)
Hawaii	2.7	96	0.3	117
St Helena	0.12	10	1.2	77
Bermuda	0.64	27	0.9	108
Cape Verde	0.20	5	8.0	140
Louisville	1.3	90	0.16	84
MacDonald	1.7	105	0.15	89
Marquesas	2.0	105	0.18	97
Society	2.5	105	0.22	108
Reunion	0.39	15	1.7	113
Juan Fernandez	0.77	65	0.18	76
Ethiopia	0.42	7	8.6	172
Asencion	0.38	40	0.24	68
Bowie	0.36	50	0.14	59
Darfur	0.19	10	1.9	96
Discovery	0.19	13	1.1	85
East Africa	0.26	12	1.8	103
Fernando	0.38	32	0.37	76
Great Meteor	0.15	4	9.4	136
Hoggar	0.12	5	4.8	108
Kerguelen	0.09	6	2.5	86
Pitcairn	0.73	100	0.07	60
San Felix	1.0	60	0.28	90
Tibesti	0.14	5	5.6	117
Trinadade	0.36	30	0.4	77
Tristan-Gough	0.22	12	1.5	95
Vema	0.17	12	1.0	83

* Swell magnitude as defined by Davies (1988).
† η_p in Pa s.

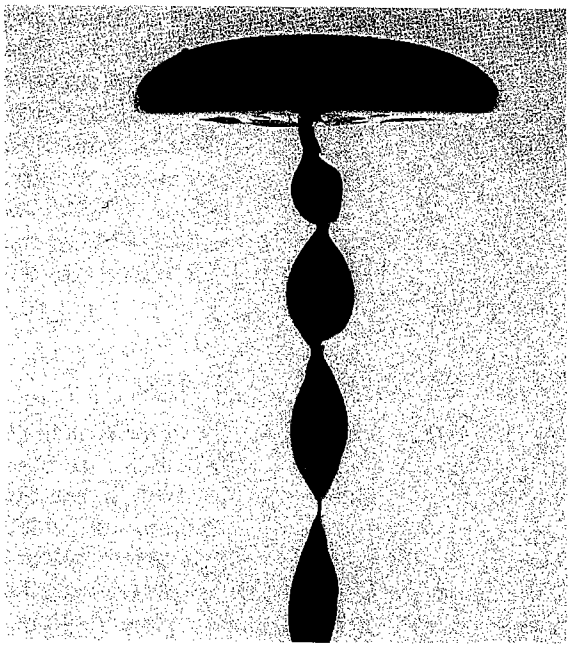

Figure 3. Intrusion of a plume-diapir structure into a cold thermal boundary layer in a temperature-dependent viscous sucrose solution. The viscosity of the matrix fluid varies from 15 000 to 150 Pa s from top to bottom. The plume fluid (alcohol–water solution) has a viscosity of 2×10^{-2} Pa s and a density contrast of 33% relative to the matrix fluid. The leading edge diapir has collapsed and spread laterally in response to the vertical viscosity gradients in the rheological boundary layer. Note the train of large-amplitude solitary waves propagating on the vertical conduit

variety of disturbances and instabilities, including *solitary waves* and *diapir chains*.

Figure 3 shows a low-viscosity plume intruding a cold, highly viscous thermo-mechanical boundary layer. A train of large-amplitude waves are seen propagating up the conduit. These waves are generated in the source region where the conduit connects with the hot thermal boundary layer. They are often present in plume conduits, even when the source strength is constant in time (Olson and Christensen, 1986; Schubert *et al.*, 1989). Conduit waves represent a possible mechanism for high-frequency variability in mantle plumes, as well as means for rapid transport of material from the source boundary layer to the surface (Whitehead and Helfrich, 1988; chapter 4, this volume).

The theory of conduit waves is based on the response of a low density, low viscosity vertical fluid conduit with a variable circular cross-sectional area A, imbedded in an infinite, homogeneous and more viscous matrix. The conduit is affected by viscous normal forces exerted on the conduit wall by the flow of the exterior matrix, which makes a contribution to the dynamic pressure in the conduit material. The expression for the vertical pressure gradient within a deforming conduit is

$$\frac{\partial P}{\partial z} = -\rho g' - \frac{\partial \tau_n}{\partial z} \tag{18}$$

where τ_n is the normal stress exerted by the mantle on the conduit wall. Flow in the conduit is assumed to obey Poiseuille's law

$$Q = -\frac{A^2}{8\pi\rho\nu_p}\frac{\partial P}{\partial z} \tag{19}$$

To first order, τ_n is proportional to the rate of contraction of the conduit, so that

$$\tau_n = -\frac{\rho\nu}{A}\frac{\partial A}{\partial t} \tag{20}$$

The model is closed by adding the continuity equation for the conduit, in the form

$$\frac{\partial A}{\partial t} = -\frac{\partial Q}{\partial z} \tag{21}$$

Writing equations (18–(20) in terms of A and Q yields

$$Q = \frac{A^2}{8\pi\nu_p}\left[g' + \nu\frac{\partial}{\partial z}\left(\frac{\partial Q}{A\partial z}\right)\right] \tag{22}$$

In the undisturbed portions of the conduit, where $A = A_0$, equation (22) reduces to the Poiseuille flow relation for buoyantly driven motion,

$$Q_0 = \frac{g' A_0^2}{8\pi\nu_p} \tag{23}$$

with the subscripts 'o' denoting the undisturbed state. Analytical solutions to equations (21) and (22) have been obtained for isolated solitary waves by Scott and Stevenson [1984] in the context of porous media flow, and by Olson and Christensen (1986) for conduit waves, of the form

$$A = A_0 + A_{max}\exp\left(\frac{-4y^2}{\lambda^2}\right) \tag{24}$$

where

$$y = z - ct \tag{25}$$

and the pulse length λ is

$$\lambda = \left(\frac{8c\nu}{g'}\right)^{1/2} \tag{26}$$

For a large disturbance, where $A_{max} \gg A_0$, the propagation speed c is related to the amplitude by

$$c = c_0 \ln (A_{max}/A_0) \quad (27)$$

in which $c_0 = 2Q_0/A_0$ is the average fluid velocity in the conduit. The dispersion relationship (27) has been demonstrated experimentally by Olson and Christensen (1986) and by Whitehead and Helfrich (chapter 4). Whitehead and Helfrich (chapter 4) also have verified that large amplitude conduit wave shapes have Gaussian profiles as given by equation (24). The effective duration of the wave pulse Δt is just

$$\Delta t = \frac{\lambda}{c} = \left(\frac{8\nu}{g'c}\right)^{1/2} \quad (28)$$

and ΔV, the volume of material transported by the wave is given by

$$\Delta V = \int_{-\infty}^{\infty} (A - A_0)\, dy = \left(\frac{2\pi c\nu}{g'}\right)^{1/2} A_{max} \quad (29)$$

Solitary waves provide a mechanism for rapid transport of buoyant material from deep in the mantle to the near-surface. As an example, using equations (28) and (29), a solitary conduit wave transporting $\Delta V = 10^{17}\,m^3$ of $\nu_p = 2 \times 10^{15}\,m^2\,s^{-1}$ material through $\nu = 2 \times 10^{18}\,m^2\,s^{-1}$ mantle within a conduit that otherwise transports only $Q_0 = 0.1\,m^3\,s^{-1}$ (a negligible amount for hot-spot tracks) has a propagation speed of approximately 17 cm year^{-1}, a 600-km wavelength and a pulse duration of approximately 7 Ma. The propagation speed is about 15 times the ascent speed of a Stokes diapir with the same volume. Intrusion of this material into the lithosphere would produce a topographic rise comparable to the leading edge of the major hot-spot swells, and enough melt to produce a flood basalt province on continental crust, or an ocean plateau on oceanic crust. Furthermore, as emphasized by Whitehead and Helfrich (1988; chapter 4, this volume), the wave consists mostly of flow within closed streamlines, so that chemically distinct material, as well

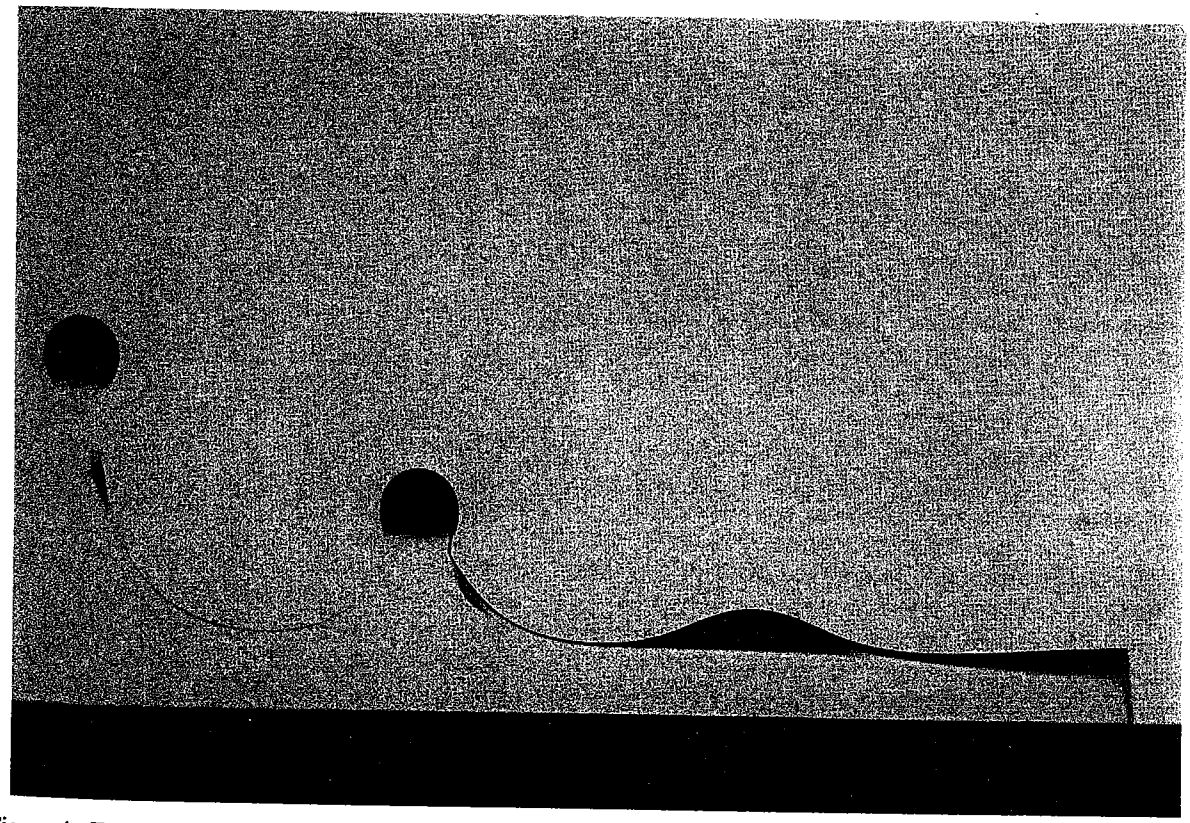

Figure 4. Formation of a diapir chain by the tilt-instability of a low viscosity plume conduit in a high viscosity matrix fluid, produced by steady relative motion between the plume source and the matrix (Olson and Singer, 1985). Plume source moves from left to right. This simulates instabilities in mantle plume conduits caused by background shear associated with plate-scale flow in the mantle. Scale units are inches.

as heat, can be advected rapidly to the lithosphere within these structures.

Conduit waves also serve as the mechanism for instability of the plume by background shear in the mantle. Figure 4 shows the formation of a diapir chain from a sheared conduit. In this case, the shear is produced by relative motion between the matrix fluid and the plume source. Whereas conduit waves propagate stably in a vertical plume, they are not stable when the plume is inclined beyond a critical angle, which is found experimentally to be approximately 60° (Whitehead, 1982). The component of the buoyancy force normal to the tilted conduit distorts the waves such that they become enlarged on the upward side. Their additional buoyancy allows them to rise above the trajectory of the conduit and to finally detach from it, forming a separate diapir. This process repeats itself in a continuously sheared conduit, producing a chain of diapirs, as shown in Figure 4. Thus, a major effect of large-scale mantle convection on plumes is expected to be the formation of diapirs by the tilt-induced instability of conduit waves.

4. Swell Formation

The most direct evidence on the structure of mantle plumes comes from hot-spot swells, which we interpret as isostatic images of plumes deflected by the lithosphere. As an ascending mantle plume approaches the lithosphere from below, its vertical velocity is reduced by the large gradient in viscosity that defines the transition from the lithosphere to the asthenosphere. Beneath *moving* lithosphere the plume trajectory is refracted into the horizontal plane. In this environment the plume shape is governed primarily by a balance between longitudinal advection by plate motion and lateral spreading driven by buoyancy. The resulting swell is governed by competition between these two effects, plus vertical heat conduction into the overlying plate. Heat conduction in the two horizontal directions is negligible in large swells, in comparison with horizontal heat advection.

Here we present a simplified model of swell formation by a refracted, buoyant mantle plume. We shall demonstrate that the combination of longitudinal advection and lateral spreading from a narrow conduit beneath the lithosphere can account for the variety of shapes found among hot-spot swells. Dynamics of this new model are fundamentally different from the standard 'heat source' model that has been used in the past to explain the evolution of swells. The heat-source model assumes that hot-spot swells are the result of conductive heat transfer to the lithosphere from a stationary, large-scale heat source in the mantle (Sandwell, 1982; Detrick *et al.*, 1986; Liu and Chase, 1989). Importantly, the heat-source model assumes that heat and buoyancy are transferred without transfer of mass. These assumptions are not consistent with the known behaviour of plume intrusion into a rheologically strong surface thermal boundary layer. Numerical and laboratory experiments (Olson *et al.*, 1988) have demonstrated that a mushroom-shaped cap forms at the top of the plume as it is incident on the lithosphere from below (see Figure 3). Growth of this structure is the primary mechanism for transmitting buoyancy from the conduit to the rheological layer. In contrast, heat conduction does not play a major role in *formation* of swells by plumes. Conduction does become significant far down the track from the conduit, where heat from the plume begins to be lost at the surface. At that point, the swell magnitude starts to decay from loss of buoyancy by surface heat conduction. The standard heat-source model explains *all* of the swell decay in terms of surface heat loss, and so predicts large heat-flow anomalies on older parts of hot-spot swells. This is in contradiction to measured heat flow on the Hawaiian Ridge, where the heat-flow anomaly is small (Von Herzen *et al.*, 1982).

The evolution of a mantle plume refracted beneath the lithosphere can be modeled in a simplified way by considering the flow of buoyant, viscous fluid from a point source located in a homogeneous, viscous asthenosphere beneath a rigidly moving plate, as illustrated in Figure 5. Pressure-driven flow from a point source in an asthenospheric channel with uniform depth has been considered previously by Sleep (1987). Here we assume that buoyancy drives the spreading of the plume relative to the moving lithosphere. For dynamical consistency, it is assumed that the viscosity of plume and the asthenosphere material are not very different. This condition justifies the model assumption that the rate of spreading is controlled by the properties of the plume material. We shall demonstrate a postiori the

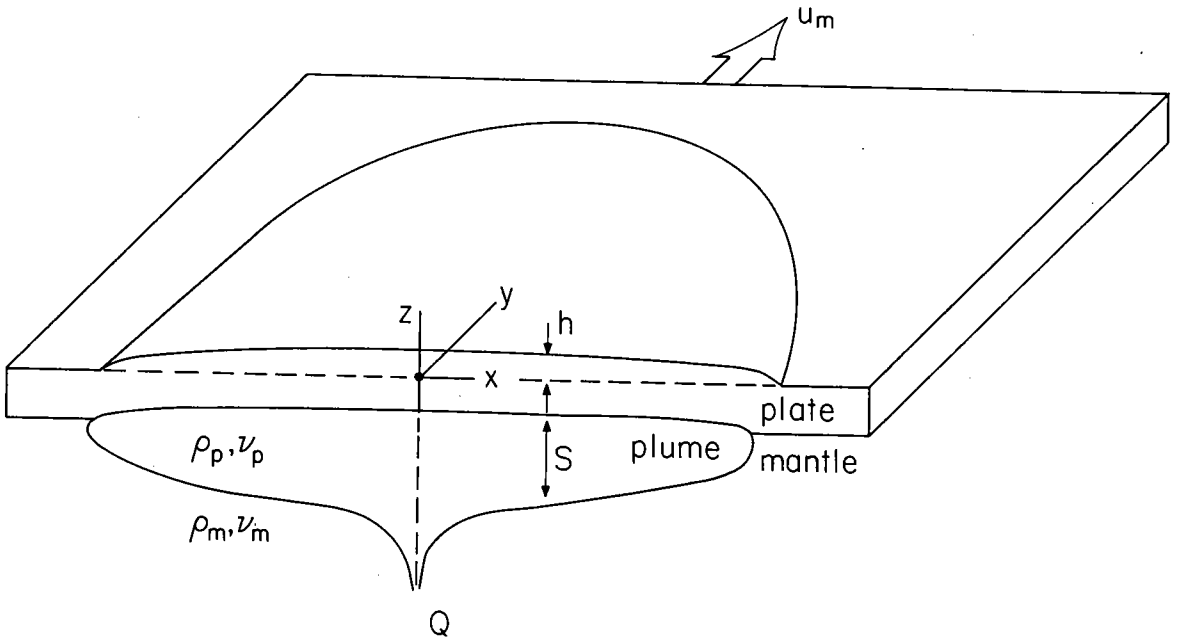

Figure 5. Sketch showing the geometry used to model hot-spot swell formation by a buoyant mantle plume spreading from a conduit source beneath a moving lithospheric plate. Plume properties are denoted by subscript p, mantle properties by subscript m. Density and kinematic viscosity are denoted by ρ and ν, respectively. Plate speed is denoted by u_m

restrictions this assumption places on the model. In addition, it is assumed, for the sake of simplicity, that the undisturbed asthenosphere moves with the plate at a velocity $\mathbf{u}_m$, and that the plume material is injected beneath the plate at a fixed point $\mathbf{x}_p$, representing a narrow, vertical, and stationary conduit source. As the plume material spreads away from the conduit, its thickness S rapidly becomes small compared with its lateral dimensions, and the flow of the plume relative to the moving plate can be modeled using the thin channel approximation. The horizontal velocity in the spreading plume $\mathbf{u}_p$ is then governed by a channel flow equation of the form

$$\frac{\partial^2 \mathbf{u}_p}{\partial z^2} = \frac{g'}{\nu_p} \nabla_H S \tag{30}$$

where z is the vertical coordinate, as shown in Figure 5, and ∇_H is the gradient with respect to horizontal coordinates. Three integrations of equation (30) vertically across the intrusion, subject to the conditions that the asthenosphere below and the plate above the intrusion move with the same velocity $\mathbf{u}_m$, yields the following expression for the horizontal plume flux $\mathbf{q}$

$$\mathbf{q} = \int_{-S}^{0} \mathbf{u}_p \, dz = \mathbf{u}_m S - \frac{g'}{48\nu_p} \nabla_H S^4 \tag{31}$$

The continuity equation for the intrusion can be written as

$$\frac{\partial S}{\partial t} = -\nabla_H \cdot \mathbf{q} + Q\delta(\mathbf{x} - \mathbf{x}_p) \tag{32}$$

in which the conduit is represented as a point source. Substitution of equation (31) into (32) yields an *intrusion equation* in terms of S

$$\frac{\partial S}{\partial t} + \mathbf{u}_m \cdot \nabla_H S = \sigma \nabla_H^2 S^4 + Q\delta(\mathbf{x} - \mathbf{x}_p) \tag{33}$$

where

$$\sigma = \frac{g'}{48\nu_p} \tag{34}$$

is the *intrusivity*. Equation (33) is made dimensionless using u_m and $(Q/2\pi u_m)^{1/2}$ as velocity and length scales. Using asterisks for dimensionless variables, equation (33) becomes

$$\frac{\partial S^*}{\partial t^*} + \hat{\mathbf{u}} \cdot \nabla_H^* S^* = I \nabla_H^{*2} S^{*4} + \delta(\mathbf{x}^* - \mathbf{x}_p^*) \tag{35}$$

where I is the *intrusion number*

$$I = \frac{g'Q}{96\pi\nu_p u_m^2} \tag{36}$$

and $\hat{\mathbf{u}}$ is the unit vector in the direction of plate motion. In terms of the swell magnitude M used by Davies (1988), the intrusion number is

$$I = \frac{gM}{96\pi\nu_p u_m^2} \tag{37}$$

From left to right, the terms in equation (35) represent the local rate of change of thickness of the intruding plume, advection of plume material by plate motion, buoyant spreading of plume material beneath the lithosphere and influx of plume material from the conduit, respectively. In a steady state, the shape of the intrusion is entirely governed by the magnitude of the intrusion number. For large values of I, corresponding to a large conduit discharge, low plume viscosity or slow plate motion, the advection term is negligible and the steady state intrusion is nearly circular. For small values of I, corresponding to either a weak plume, fast plate motion or high asthenospheric viscosity, advection dominates over spreading and the steady state intrusion is an elongated ridge. The isostatic topography above the intrusion is just

$$h = \frac{\Delta\rho}{\rho - \rho_w} S \tag{38}$$

where $\Delta\rho = \rho - \rho_p$ is the plume density deficit relative to the mantle and ρ_w is sea-water density. The associated isostatic geoid height anomaly is given by

$$\Delta N = \frac{\pi G \Delta\rho Z S}{g}\left(\frac{S}{Z} + 2\right) \tag{39}$$

where G is the gravitational constant and Z is the plate thickness. The ratio of geoid height to topography is constant over most of the swell, and is equal to

$$\frac{\Delta N}{h} \simeq \frac{2\pi G \Delta\rho Z}{g} \tag{40}$$

Since much of the hot-spot swell topography is supported isostatically, the shape of the swell approximates the shape of the horizontally refracted plume. Thus, a first order model for swells produced by a refracted plume is obtained by rescaling the solution to equations (33) or (35) according to equation (38), using an assumed plume-density anomaly $\Delta\rho$. It is important to emphasize that this is not a good model for topography and geoid in the immediate neighborhood of a plume conduit where the topography is influenced by dynamic support and by flexure of the lithosphere, and the geoid is not isostatic.

In order to test the refracted plume model, estimates are needed of the intrusion number for major hot-spot swells. Table 1 lists the characteristics of 26 hot-spot swells as compiled by Davies (1988). Also listed is the intrusion number for each swell, in units of $10^{20}/\eta_p{}^{-1}$, where η_p is the dynamic viscosity of the plume in Pa s. While there is a range of intrusion numbers in Table 1, most values fall within one of two groups. The majority of swells have intrusion numbers less than 1, assuming the plume viscosity is of the order 10^{20} Pa s. This category includes all the high magnitude swells associated with Pacific hot spots. Most of the hot spots within this group have well defined, elongate tracks and ridge-shaped swells (Crough, 1978). The other recognizable group, represented by the Cape Verde, Ethiopia and Tibesti hot-spots, have intrusion numbers 10–50 times larger than the first group. The swells associated with these hot spots are more dome-like, as opposed to ridge-like. Also listed in Table 1 are values of L, the internal length-scale for each swell,

$$L = \left(\frac{\rho M}{2\pi\Delta\rho u_m}\right)^{1/2} \tag{41}$$

calculated assuming $\Delta\rho/\rho = 0.01$.

Numerical solutions to equation (35) have been computed in order to demonstrate that the variety of shapes among hot-spot swells can be accounted for by differences in the intrusion number, as given in Table 1. The numerical solutions were obtained on 40×40 and 80×40 finite difference grids, using an explicit time-step procedure. The conduit source $\mathbf{x}_p$ was fixed midway between the grid points $(i,j) = (15,20)$ and $(16,20)$, where i and j are the longitudinal and lateral indices, respectively. The source strength was prescribed by applying the condition

$$(\mathbf{x}^* - \mathbf{x}_p^*) \cdot (\hat{\mathbf{u}}S^* - I\nabla_H^* S^{*4}) = 1 \tag{42}$$

at the grid points surrounding the source point. A zero-flux condition

$$\frac{\partial S^*}{\partial n} = 0 \tag{43}$$

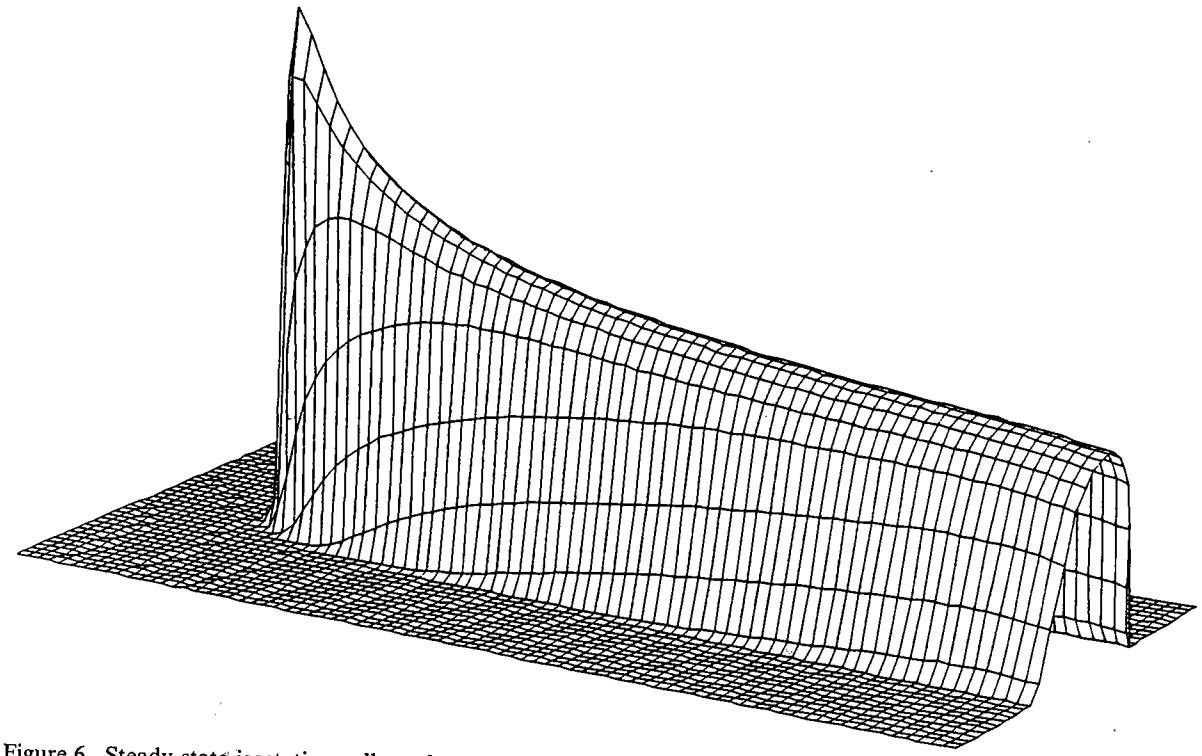

Figure 6. Steady state isostatic swell produced by a buoyant plume refracted beneath a moving plate, calculated at intrusion number $I = 0.1$. Maximum height is 3.4 length-scales; the grid is 20×40 length-scales. One length-scale is approximately 100 km. The direction of plate motion is from left to right

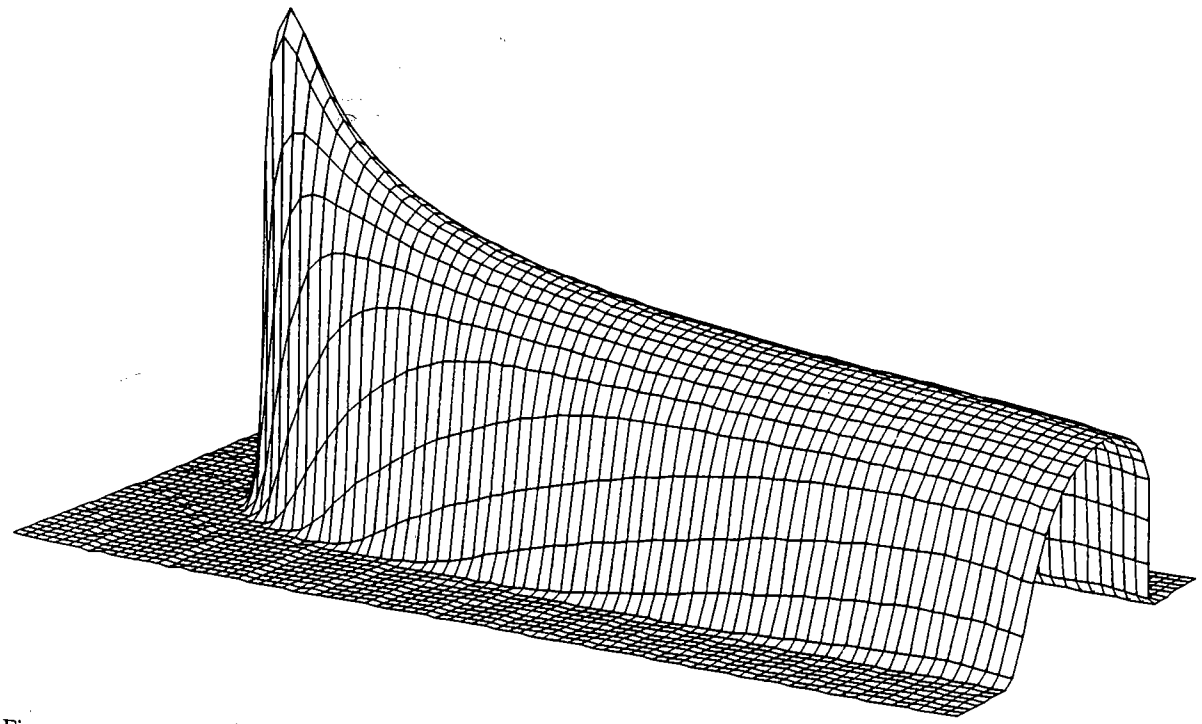

Figure 7. Steady state isostatic swell produced by a buoyant plume refracted beneath a moving plate, calculated at intrusion number $I = 0.3$. Maximum height is 2.6 length-scales; the grid is 20×40 length-scales

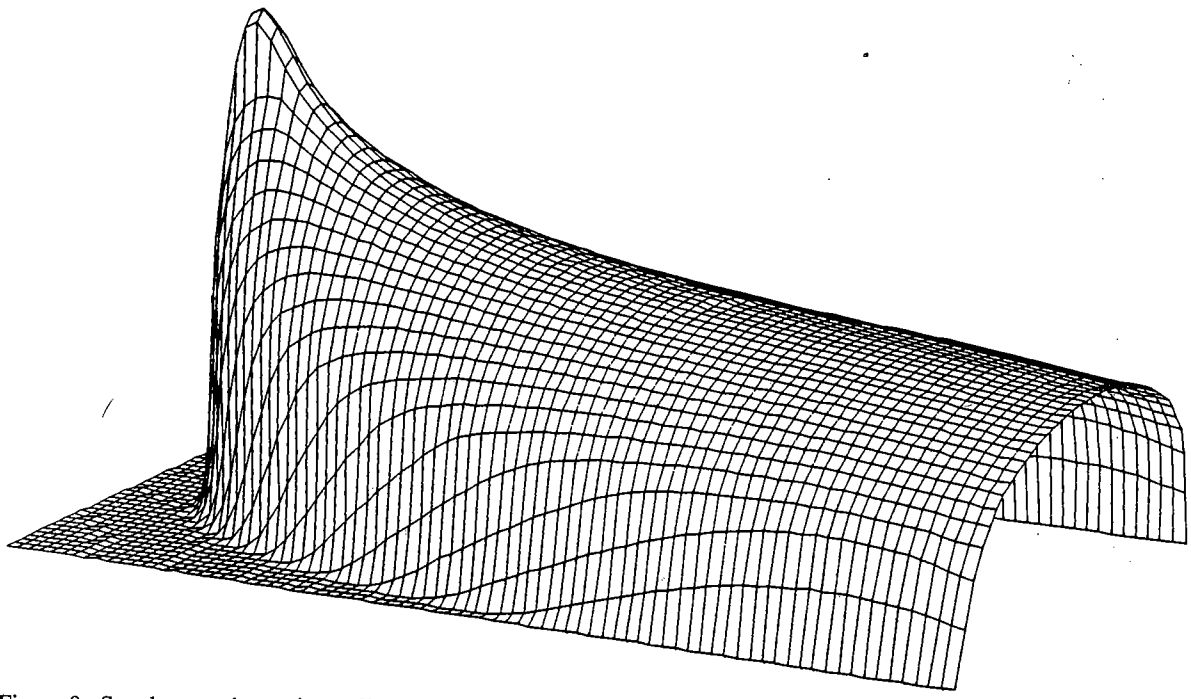

Figure 8. Steady state isostatic swell produced by a buoyant plume refracted beneath a moving plate, calculated at intrusion number $I = 1.0$. Maximum height is 1.9 dimensionless length-scales; the grid is 20×40 length-scales. Note the increase in lateral spreading with increasing intrusion number in Figures 6–8

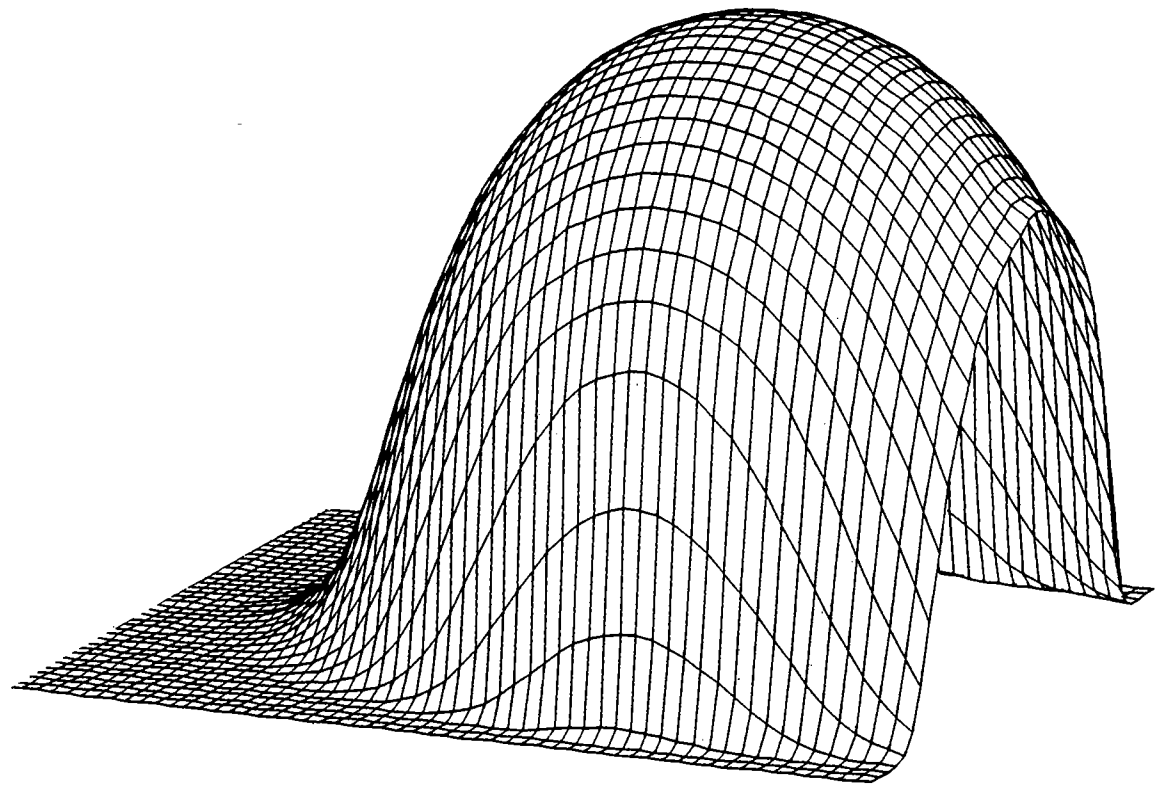

Figure 9. Isostatic swell produced by a transient plume source refracted beneath a moving plate, calculated at intrusion number $I = 10$. Maximum height is 1.2 dimensionless length-scales; the grid is 80×80 length-scales

where n is normal to the boundary, was applied at the downstream edge of the grid.

Figures 6–8 show steady state distributions of S^* calculated for intrusion numbers $I = 0.1$, 0.3 and 1.0, respectively. The direction of plate motion is from left to right. Figure 9 shows the distribution of S^* after 50 time units, calculated for $I = 10$ with a transient source, active for 40 time units. Note that the pointed crest present in the steady state swells has decayed in this case. In Figure 6–8, the grid represents an area 20×40 length-scales, and the grid in Figure 9 represents an area 80×80 in length-scales. The maximum value of S^* is given in the figure captions. These images are proportional to the isostatic topography, by virtue of equation (38).

The swell structure varies from a narrow ridge to a slightly asymmetric dome over this range of intrusion numbers. At $I = 0.1$ (Figure 6), advection by the moving plate dominates over lateral spreading and the swell forms a narrow ridge, only eight length-scales wide where it exits the grid. The decay in swell height is correspondingly slow. The leading edge of the swell is only about two length-scales ahead of the conduit. In the most diffuse case, with $I = 10$ (Figure 9), the

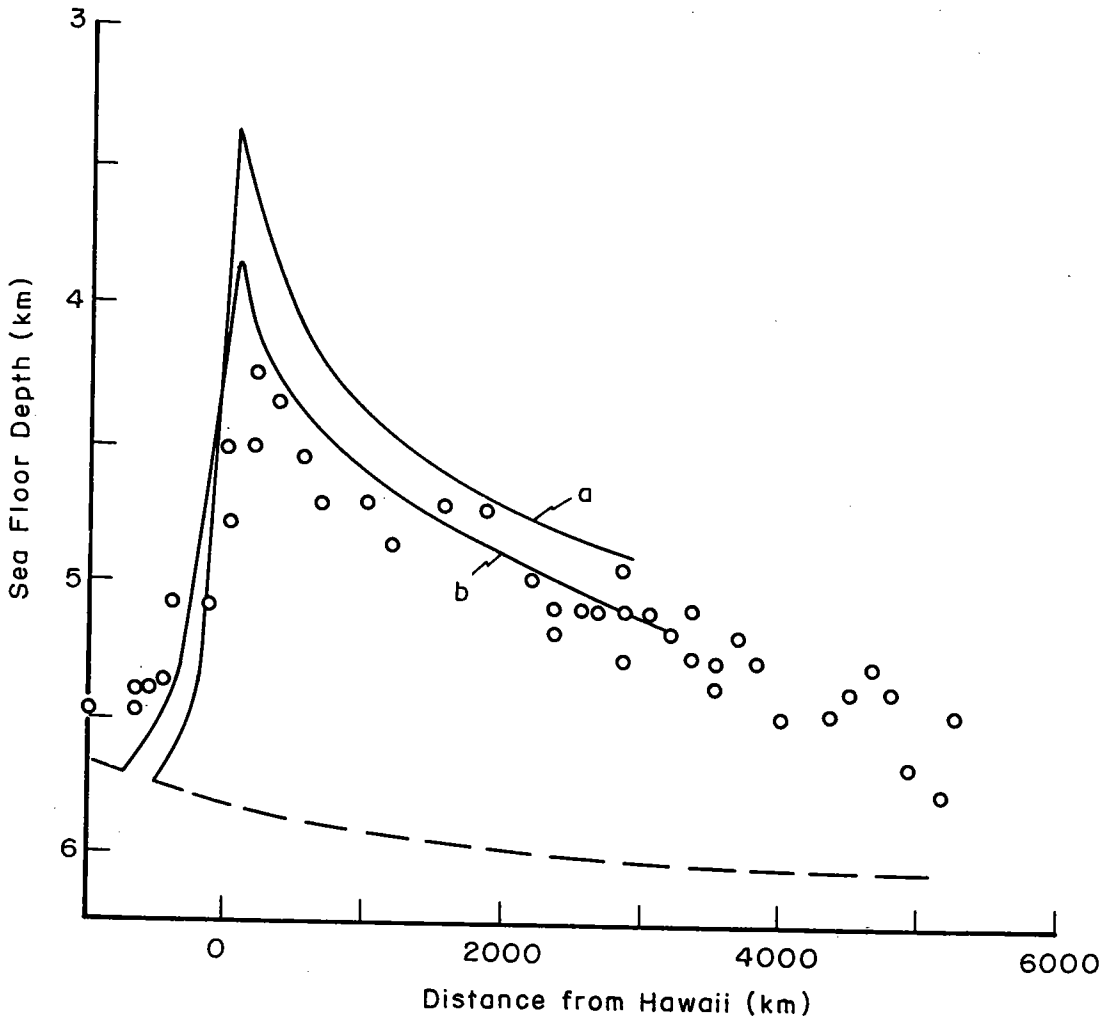

Figure 10. Axial isostatic topography versus distance along the swell track due to a plume spreading from a steady point source, refracted beneath a moving plate, calculated at intrusion numbers $I = 0.3$ (a) and 1.0 (b). The topography is relative to the normal sea-floor depth predicted by conductive cooling (dashed curve), with 80-Ma ocean crust at the hot-spot source point. The calculation uses the following parameter values: length-scale $L = 100$ km; plume viscosity $\eta_p = 10^{20}$ Pa s; plume buoyancy $g' = 0.1$ m s^2. Data points are the axial topography along the Hawaiian Ridge from Crough (1978)

swell is a broad dome, slightly elongated in the direction of plate motion. Here the swell is 50 length-scales wide. Cases with intermediate diffusion numbers (Figures 7 and 8) result in swells with shapes intermediate between these two extremes.

In order to scale these results to mantle plumes, we note that the length-scales L in Table 1 are of the order of 100 km for all hot spots listed. Using this value as the nominal length-scale, the maximum widths in Figures 6–9 are 800, 1000, 2000 and 5000 km, respectively, and the maximum plume thicknesses, S_{max}, are 340, 260, 190 and 130 km, respectively. The solutions for $I = 0.3$ (Figure 7) and 1.0 (Figure 8) bracket the width of the major hot-spot swells in the Pacific. Both cases yield elongated ridge-shaped swells that are morphologically similar to the swells with small intrusion numbers in Table 1. Thus it appears that the intrusion number for ridge-shaped swells is in the range 0.3–1.0. Intrusion numbers in this range are consistent with the data for ridge-shaped swells in Table 1 provided the average viscosity in the spreading plume is approximately $\eta = 10^{20}$ Pa s, essentially the same as inferred for the upper mantle from post-glacial rebound. This consistency justifies the model assumption that the viscosity in the spreading plume is not much less than the viscosity of the asthenosphere; however, it is larger than usually inferred for plumes in the deep mantle, as in section 3.

As a further test of the model, the calculated isostatic topography is compared with the topography along the crest of the Hawaiian swell. Figure 10 shows Hawaiian-swell elevation data from Crough (1978), plus the axial isostatic topography derived from the steady state solutions with $I = 0.3$ and 1.0 (Figures 7 and 8), obtained by assuming $L = 100$ km and $(\rho - \rho_p)/(\rho - \rho_w) = 0.01$ in equations (38) and (41). The assumed density anomaly corresponds to an average temperature excess of about 200 K in the refracted plume. The peak elevations are larger in the model than observed, because the model source is a δ-function and because flexure of the lithosphere is not included in the calculation. In addition, the calculated swells do not extend as far uptrack as the data indicates, although this may also be simply a consequence of the point-source assumption. More significantly, the decay of swell height with distance downtrack from the conduit source is similar to the observed decay, to a distance of 3000 km, where the computational grid ends. It is important to emphasize that the decrease in swell height in this model is a consequence of lateral spreading, and not a consequence of surface heat loss, as is assumed in the standard heat-source model. Conductive heat loss certainly contributes to swell decay, but is not the only mechanism responsible. Indeed, the numerical examples given here indicate that buoyantly driven lateral spreading, which has not been considered in previous models of swell evolution, may be the most important factor.

Acknowledgements

This research has been supported by grant NAG 5152 from NASA and the Experimental and Theoretical Geophysics program of NSF.

References

Bargar, K.E. and Jackson, E.D. (1974). Calculated volumes of individual shield volcanoes along the Hawaiian–Emperor chain. *J. Res. U.S. Geol. Survey*, **2**, 545–550.

Basaltic Volcanism Study Project (1981). *Basaltic Volcanism on the Terrestrial Planets*. Pergamon Press, NY, 1286 pp.

Bercovici, D., Schubert, G., and Glatsmaier, G.A. (1989). Three-dimensional, large-scale convection in the Earth's mantle. *Science*, **244**, 950–955.

Chase, C.G. (1981). Oceanic island Pb: two-stage histories and mantle evolution. *Earth Planet. Sci. Lett.*, **52**, 277–284.

Christensen, U. (1984). Instability of a hot thermal boundary layer and initiation of thermo-chemical plumes. *Anal. Geophys.*, **2**, 311–320.

Crough, S.T. (1978). Thermal origin of mid-plate hot-spot swells. Geophys. *J. R. Astron. Soc.*, **55**, 4451–4469.

Davies, G.F. (1988). Ocean bathymetry and mantle convection, 1. Large-scale flow and hotspots. *J. Geophys. Res.*, **93**, 10467–10480.

Detrick, R.S., Von Herzen, R.P., Crough, S.T., Epp, B., and Fehn, U. (1981). Heat flow on the Hawaiian swell and lithospheric reheating. *Nature*, **292**, 142–143.

Detrick, R.S., Von Herzen, R.P., Parsons, B., Sandwell, D., and Dougherty, M. (1986). Heat flow observations on the Bermuda rise and thermal models of midplate swells. *J. Geophys. Res.*, **91**, 3701–3723.

Hager, B.H. (1984). Subducted slabs and the geoid: constraints on mantle rheology and flow. *J. Geophys. Res.*, **89**, 6003–6015.

Hansen, U. and Yuen, D.A. (1988). Numerical simulations of thermal-chemical instabilities at the core–mantle boundary. *Nature*, **334**, 237–240.

Hart, S.R., Gerlach, D.C., and White, W. M. (1986). A possible new Sr–Nd–Pb mantle array and consequences for mantle mixing. *Geochim. Cosmochim. Acta*, **50**, 1551–1563.

Hofmann, A.W. and White, W.M. (1982). Mantle plumes from ancient oceanic crust. *Earth Planet. Sci. Lett.*, **57**, 421–436.

Howard, L.N. (1964). Convection at high Rayleigh number. In Gortler, H. (ed.) *Proceedings of the 11th International Congress on Applied Mechanics*, Munich. Springer, Berlin, 1109–1115.

Jeanloz, R. and Morris, S. (1986). Temperature distribution in the crust and mantle. *Ann. Rev. Earth Planet. Sci.*, **14**, 377–415.

Jurdy, D.M. and Gordon, R.G. (1984). Global plate motions relative to the hotspots 64 to 56 Ma. *J. Geophys. Res.*, **89**, 9927–9936.

Liu, M. and Chase, C.G. (1989). Evolution of midplate hotspot swells: numerical simulation. *J. Geophys. Res.*, **94**, 5571–5584.

Loper, D.E. (1985). A simple model of whole mantle convection. *J. Geophys. Res.*, **90**, 1809–1836.

Machetel, P. and Yuen, D.A. (1986). The onset of time-dependent convection in spherical shells as a clue to chaotic convection in the Earth's mantle. *J. Geophys. Res.*, **13**, 1470–1473.

Molnar, P. and Stock, J. (1987). A revised Early Tertiary history of plate motion in the southwest Pacific. *Nature*, **327**, 587–591.

Morgan, W.J. (1981). Hotspot tracks and the opening of the Atlantic and Indian Oceans. In: Emiliani, C. (ed.) *The Sea*, Vol. 7. Wiley-Interscience, NY, pp. 443–487.

Morgan, W.J. (1983). Hotspot tracks and the early rifting of the Atlantic. *Tectonophysics*, **94**, 123–139.

Olson, P. and Christensen, U. (1986). Solitary wave propagation in a fluid conduit within a viscous matrix. *J. Geophys. Res.*, **91**(B), 6367–6374.

Olson, P. and Singer, H. (1985), Creeping plumes. *J. Fluid Mech.*, **158**, 511–531.

Olson, P., Schubert, G., and Anderson, C. (1987). Plume formation in the D"-layer and the roughness of the core–mantle boundary. *Nature*, **327**, 409–413.

Olson, P., Silver, P.G., and Carlson, R.W. (1989). The large-scale structure of convection in the Earth's mantle. *Nature*, **344**, 209–215.

Olsen, P., Schubert, G., Anderson, C., and Goldman, P. (1988). Plume formation and lithosphere erosion: a comparison of laboratory and numerical experiments. *J. Geophys. Res.*, **93**, 15065–15084.

Richards, M.A. Duncan, R.A., and Courtillot, V.E. (1989). Flood basalts and hotspot tracks: plume heads and tails. *Science*, submitted.

Richter, F.M. and McKenzie, D.P. (1981). On some consequences and possible causes of layered mantle convection. *J. Geophys. Res.*, **86**, 6124–6133.

Sandwell, D.T. (1982). Thermal isostacy: response of a moving lithosphere to a distributed heat source. *J. Geophys. Res.*, **87**, 1001–1014,

Sandwell, D. and MacKenzie, K.R. (1989). Geoid height versus topography for oceanic plateaus and swells. *J. Geophys. Res.*, **94**, 7403–7418.

Schubert, G., Olson, P., Anderson, C., and Goldman, P. (1989). Solitary waves in mantle plumes. *J. Geophys. Res.*, **94**, 9523–9532.

Scott, D.R. and Stevenson, D.J. (1984). Magma solitons. *Geophys. Res. Lett.*, **11**, 1161–1164.

Silver, P.G., Carlson, R.W., and Olson, P. (1988). Deep slabs, geochemical heterogeneity and the large-scale structure of mantle convection. *Ann. Rev. Earth Planet. Sci.*, **16**, 477–541.

Singer, H. (1986). *Heat transport by steady state plumes with strongly temperature-dependent viscosity*. PhD Thesis, The Johns Hopkins University, Baltimore Md., 194 pp.

Sleep, N. (1987). Lithospheric heating by mantle plumes. *Geophys. J. R. Astron. Soc.*, **91**, 1–11.

Vogt, P.R. (1979). Global magmatic episodes: new evidence and implications for the steady-state mid-ocean ridge. *Geology*, **7**, 93–98.

Von Herzen, R.P., Detrick, R.S., Crough, S.T., Epp, D., and Fehn, U. (1982). Thermal origin of the Hawaiian Swell: heat flow evidence and thermal models. *J. Geophys. Res.*, **87**, 6711–6723.

White, R. and McKenzie, D.P. (1989). Magmatism at rift zones: the generation of volcanic continental margins and flood basalts. *J. Geophys. Res.*, **94**, 7685–7730.

Whitehead, J.A. (1982). Instabilities of fluid conduits in a flowing earth—are the plates lubricated by the asthenosphere? *Geophys. J. R. Astron. Soc.*, **70**, 415–433.

Whitehead, J.A. and Helfrich, K.R. (1988). Wave transport of deep mantle material. *Nature*, **336**, 59–61.

Whitehead, J.A. and Luther, D.S. (1975). Dynamics of laboratory diapir and plume models. *J. Geophys. Res.*, **80**, 705–717.

Young, C.J. and Lay, T. (1987). The core–mantle boundary. *Ann. Rev. Earth Planet. Sci.*, **15**, 25–46.

Zindler, A. and Hart, S.R. (1986). Chemical geodynamics. *Ann. Rev. Earth Planet. Sci.*, **14**, 493–571.